

Removal Mechanism and Defect Characterization for Glass-Side Laser Scribing of CdTe/CdS Multilayer in Solar Cells

Hongliang Wang¹

Department of Mechanical Engineering,
Columbia University,
New York, NY 10027
e-mail: hw2288@columbia.edu

Y. Lawrence Yao

Department of Mechanical Engineering,
Columbia University,
New York, NY 10027

Hongqiang Chen

Laser and Metrology System Lab,
GE Global Research,
Niskayuna, NY 12309

Laser scribing is an important manufacturing process used to reduce photocurrent and resistance losses and increase solar cell efficiency through the formation of serial interconnections in large-area solar cells. High-quality scribing is crucial since the main impediment to large-scale adoption of solar power is its high-production cost (price-per-watt) compared to competing energy sources such as wind and fossil fuels. In recent years, the use of glass-side laser scribing processes has led to increased scribe quality and solar cell efficiencies; however, defects introduced during the process such as thermal effect, microcracks, film delamination, and removal uncleanliness keep the modules from reaching their theoretical efficiencies. Moreover, limited numerical work has been performed in predicting thin-film laser removal processes. In this study, a nanosecond (ns) laser with a wavelength at 532 nm is employed for pattern 2 (P2) scribing on CdTe (cadmium telluride) based thin-film solar cells. The film removal mechanism and defects caused by laser-induced micro-explosion process are studied. The relationship between those defects, removal geometry, laser fluences, and scribing speeds are also investigated. Thermal and mechanical numerical models are developed to analyze the laser-induced spatiotemporal temperature and pressure responsible for film removal. The simulation can well-predict the film removal geometries, transparent conducting oxide (TCO) layer thermal damage, generation of microcracks, film delamination, and residual materials. The characterization of removal qualities will enable the process optimization and design required to enhance solar module efficiency. [DOI: 10.1115/1.4030935]

Keywords: glass-side laser scribing, micro-explosion, multilayer thin films, CdTe, solar cell

1 Introduction

Thin-film solar cell technology promises to achieve a significant cost reduction in materials, by adopting large-area deposition capability, and the use of cheap and flexible substrates. Typical thin-film solar cells used in terrestrial photovoltaic (PV) applications consist of back contact, absorber, and front contact films. CdTe is the dominant absorber material in recent years because of its attractive price and stable performance at high temperatures [1,2]. The efficiency of thin-film solar panels, however, is hampered by resistive losses in the module proportional to the square of the photocurrent. In practice, photocurrent is decreased by scribing the solar module into a large number (between 100 and 200) minimodules and connecting them in series to create high-voltage, low-current devices [3]. Since each layer in the solar module must be scribed after deposition, scribing is performed in three steps—patterns 1, 2, and 3 (P1, P2, and P3) processes, which are also used in the commercial production of a-Si:H (hydrogenated amorphous silicon) and CI(G)S (copper indium gallium selenide) based thin-film solar cell fabrications [4–6]. Compared to mechanical scribing, key advantage of laser scribing is able to enable much smaller line width (50 μm versus 500 μm), so the “dead zone” can be much smaller with higher efficiency. Also, it is currently the only industrial standard process for high-speed mass production (scribing speed around 1 m/s versus 0.05–0.1 m/s). However, laser scribing has been shown to leave a heat-affected

zone around the scribe, which causes undesirably poor isolation between cells and low-shunt resistance. Laser scribing has also been shown to leave high-protruded ridges along the edge of the scribe line, contributing to electrical shorts [4]. While scribing reduces resistive losses by decreasing photocurrent, it also forms dead zones between P1 and P3 slots, which contribute to reductions in module efficiency [7].

In order to decrease the thermal effect of laser irradiation during processing, the use of ultrashort pulsed lasers, such as picosecond and femtosecond lasers, is being investigated for scribing processes [8,9]. These lasers are complex and expensive, and regardless of pulse duration, material melting cannot be totally avoided [5]. Glass-side laser processing [10,11] has been shown to be more efficient than film side processing with reduced thermal effect. Film side laser scribing is governed by heating, melting, and vaporizing of selective films, while glass-side laser scribing is a thermal-mechanical process which involves stress induced material failure and removal rather than vaporization. The mechanical fracture and removal of film material during glass-side scribing are commonly referred to as lift off or micro-explosion processing [7]. During micro-explosion processing, the laser irradiates through the transparent substrate and is fully absorbed in a very thin layer of film at the interface. High-pressure plasma is generated and expanded in the film. The plasma punches through the solid film above and the material is removed mechanically [12]. Micro-explosion processing is pronounced when the laser material penetration depth is much shallower than the film thickness, such as P2/P3 processes of CdTe and a-Si:H solar cells. Otherwise, films are removed through thermal ablation, such as P1 process for front contact films made by TCO materials [13].

¹Corresponding author.

Contributed by the Manufacturing Engineering Division of ASME for publication in the JOURNAL OF MANUFACTURING SCIENCE AND ENGINEERING. Manuscript received August 1, 2014; final manuscript received June 21, 2015; published online September 9, 2015. Assoc. Editor: Robert Gao.

While glass-side laser scribing has led to improved scribe quality over competing methods, defects such as thermal effect, film delamination, scribe uncleanliness, and microcracks that lead to decreased module efficiency are still introduced [14,15]. Although extensive work has been carried out for optimizing the scribing qualities [4–13], the physical phenomena responsible for film removal during laser scribing and their effects on scribe quality are still not well known. In addition, development of simulation capabilities will enable the fundamental understanding of the physical mechanisms and optimize the scribing processes instead of relying on trial-and-error experiments. To date, only rudimentary modeling efforts have been made, offering no predictive or optimization capabilities. Wang et al. [13] developed a two-dimensional thermal model to estimate the temperature distribution of CdTe-based thin-film solar cells by ns (nanosecond) laser pulses irradiated from the glass side, and simulated the film removal during micro-explosion process. However, the model did not consider the dynamic response of brittle materials during this high-velocity shock wave impact, and it also offered no experimental validations.

Based on the current thin-film solar cell technology, a 1% increase in efficiency from improved scribe quality equates to roughly a 10% cost reduction. Therefore, understanding the film removal mechanisms and characterizing the potential defects during laser scribing processes are important for the cost reduction of thin-film solar cells. In the previous work [13], P1 scribing of TCO layer has been studied. P2 and P3 are similar processes, since both are under micro-explosion mechanism with the plasma occurs at the interface between absorber and TCO layers. In this study, P2 scribing of CdTe-based solar cells is carried out using a 532 nm-wavelength 9 ns-pulse-duration laser irradiated from glass side at different fluences and scribing speeds, and the corresponding scribe geometry, induced defects, and the sheet resistance of TCO layer after scribing are characterized. A two-dimensional numerical model, implemented with dynamic response of brittle material, is developed to simulate film removal via a micro-explosion process. The scribe geometry is studied by scanning electron microscopy (SEM) and optical profilometry, and removal cleanliness is estimated by energy-dispersive X-ray spectroscopy (EDX). The sheet resistance is measured through four-point probe method. Film microstructures and laser-induced defects are characterized by transmission electron microscopy (TEM).

2 Background

2.1 Laser-Induced Defects and Their Effects on Solar Cells. Laser processing has been incorporated into many successful modifications of the properties of semiconductor materials in solar cells applications. For example, Tull et al. [16] and Wang et al. [17,18] have reported laser surface texturing induced optical property change of crystalline silicon and amorphous silicon. Compaan and Matulionis [4] have investigated laser scribing on different contact and absorber layers in order to change their electrical property. However, the quality of the laser treatment is often limited by the generation of defects, which have adverse effects on solar cell performance through increased junction shunting or recombination centers. Due to the unique mechanical fracture caused by the micro-explosion process, defects as atomic structural change, microcracks/voids, and film delamination are induced resulting in poor photocurrent and inactive cells. Incomplete film removal is also observed causing an increase in contact resistance between the metal and TCO layers, which leads to less output power [19]. Lauzurica et al. [20] reported the formation of irregular scribe boundaries and observed film peeling after ns-pulsed, P3 laser scribing of a-Si thin-film solar cells. Tamaoki et al. [21] showed the formation of microcracks and film delamination after scribing of a molybdenum film on a glass substrate using an ns-laser. Even the use of ultrashort pulse-duration lasers has not shown the ability to eliminate defects such as film delamination [8]. Kontgers et al. [15] have investigated the risk of power

loss, up to 10%, in PV modules due to microcracks induced inactive cells, and pointed out that the microcracks can be continually opened up subjected to the mechanical and thermal stress. Acciani et al. [22] have examined the abnormal heating in the restricted area of solar cells due to the presence of defects, such as voids, causes hotspots, and the increased temperature will introduce dead cells in the solar panel.

Defects generation can also be introduced by laser-induced thermal effect. Golovan et al. [23] investigated the defect formation in CdTe under laser-induced melting process and showed a decrease of photorefectance due to the formation of electrically and recombination active defects. In addition, when the laser power density is high enough, the TCO layer underneath the absorber will be thermally damaged as well, which could lead to shunt resistance decrease and current leakage. Furthermore, when the laser photon energy is higher than the band gap of semiconductors, defect formation of recombination centers can be also introduced even at low-laser fluences (less than the melting threshold). Emel'yanov and Kashkarov [24] showed that the fraction of the energy of the photo-excited electron-hole pairs is transferred in the process of electron-phonon relaxation and heat the lattice. The strong rise in temperature T (up to melting point) leads to the generation of defects by thermofluctuation, which is frozen in after the end of the pulse due to the very rapid cooling process. The density of the thermofluctuation defects reaches its stationary value

$$N_d = \text{const} \cdot \exp\left[-\frac{E_A}{K(T_0 + \Delta T)}\right] \quad (1)$$

where T_0 is the initial temperature, ΔT is the temperature rise due to laser heating, E_A is the defect formation energy, and K is Boltzmann constant. This equation describes the generation of vacancies (Schottky defects), the annihilation, and the formation of defect complexes and other defects [24]. The lattice deformation caused by the heating reduces the value of the defect activation energy in Eq. (1). The defect formation energy can also be reduced due to the localization of the electronic energy in some point of the crystal, which will decrease the potential barrier of the defect transition to a new equilibrium position. Thus, the localization of the electronic excitation on some initial defect can introduce new centers due to the process of defect multiplication.

2.2 Dynamic Response of Brittle Materials. Due to the short duration of the laser pulse, film removal always occurs in nanosecond scales. This high-velocity pressure impact on CdTe will cause a high-strain rate during laser scribing. Therefore, an assessment of the inelastic behavior including strain-rate phenomena, material degradation, and pressure hardening needs to be considered. Micromechanical-based approach typically starts with the behavior of a single defect (crack or void), and the continuum level model is obtained by applying statistical averaging to an ensemble of defects [25]. Johnson and Holmquist (JH) [26,27] reported extensive work on brittle material response to high-velocity impacts. The JH models use experimental data to determine constants that describe inelastic material behaviors in the simulation, and they are more convenient to be implemented in finite-element models than the theoretical statistical calculation.

There are two variations of the JH models. Compared to the first version (JH-1), the second version (JH-2) incorporates a damage evolution rule by consideration of progressive damage with increasing deformation, which is more accurate for simulating the high-velocity impact performance of ceramics [26]. In JH-2 model, the strength of the material is expressed in terms of the normalized von Mises equivalent stress as

$$\sigma^* = \sigma_i^* - D(\sigma_i^* - \sigma_f^*) \quad (2)$$

where σ_i^* is the normalized intact equivalent stress, σ_f^* is the normalized fractured equivalent stress, and D is the damage variable.

The normalized equivalent stresses (σ^* , σ_i^* , σ_f^*) have the general form $\sigma^* = \sigma/\sigma_{\text{HEL}}$, where σ is the actual von Mises equivalent stress, and σ_{HEL} is the equivalent stress at the Hugoniot elastic limit (HEL). The model assumes that the normalized intact and fractured stress can be expressed as function of the pressure and strain rate as

$$\sigma_i^* = A(p^* + T^*)^N [1 + C \ln \dot{\epsilon}^*] \leq \sigma_i^{\text{max}} \quad (3)$$

$$\sigma_f^* = B(p^*)^M [1 + C \ln \dot{\epsilon}^*] \leq \sigma_f^{\text{max}} \quad (4)$$

where A , B , C , M , and N are material constants, σ_i^{max} and σ_f^{max} are the optional limits. The normalized pressure, p^* , and normalized maximum tensile hydrostatic pressure, T^* , are defined as $p^* = p/p_{\text{HEL}}$ and $T^* = T/P_{\text{HEL}}$, where P , P_{HEL} , and T are the actual pressure, pressure at the HEL, and maximum tensile pressure that the material can withstand.

The damage initiation parameter, ω , accumulates with plastic strain according to

$$\omega = \sum \frac{\Delta \epsilon^p}{\epsilon_f^p(P)} \quad (5)$$

where $\Delta \epsilon^p$ is the increment in equivalent plastic strain, and $\epsilon_f^p(P)$ is the equivalent plastic strain to fracture under constant pressure, defined as $\epsilon_f^p = D_1(P^* + T^*)^{D_2}$, where D_1 and D_2 are constants. JH-2 model assumes that the damage variable increases gradually with plastic deformation by setting $D = \omega$.

The equations for the pressure–density are described as

$$p(\zeta) = k_1 \zeta + k_2 \zeta^2 + k_3 \zeta^3 + \Delta p; \text{ compression} \quad (6)$$

$$p(\zeta) = k_1 \zeta; \text{ tension} \quad (7)$$

where $\zeta = \rho/\rho_0 - 1$ and Δp is an increment in the pressure, and k_1, k_2, k_3 are material constants. The increment in pressure arises from the conversion of energy loss due to damage into internal energy.

3 Experimental Setup

Polycrystalline TCO (SnO₂:F) films were deposited on a 3.2 mm-thick soda lime substrate using chemical vapor deposition at 600 °C. Stack layers of polycrystalline CdS and CdTe were then sequentially thermally evaporated at 350 °C substrate temperature. Film thicknesses of TCO, CdS, and CdTe layers were about 400 nm, 200 nm, and 2 μm, respectively.

Experiments were carried out using a Nd:YAG laser with 532 nm of wavelength. The system delivered 9-ns pulses at a 100 Hz repetition rate. The samples were cleaned with acetone in an ultrasonic cleaner for 5 min and then rinsed with methanol and distilled water prior to processing. The sample was placed inside a metallic container sealed with quartz at both top and bottom to avoid hazardous plume during laser processing and collect the removed materials. This container was mounted on a three-axis translation stage, and samples were irradiated by laser focused by a 20 × objective lens. The focal plane was placed at the interface between TCO and CdS to create a circular beam spot with a diameter of around 50 μm. The samples were irradiated from the glass side by single pulse with various fluences from 0.4 to 6 J/cm² at a stationary spot, and then scribed with the fluence values from 1 to 4 J/cm² at different speeds (1 to 4 mm/s). Regarding to the sheet resistance measurement, scribing areas of 5 mm × 20 mm were processed under different fluences (1 to 6 J/cm²), a scribing speed of 2 mm/s, and 50% overlap between each scribing lines.

The treated samples were observed through SEM. Surface roughness and scribe profiles were measured by optical profilometry. The chemical components and cleanliness of laser processed samples were investigated by EDX. The sheet resistance was

measured through four-point probe method. The generation of defects such as material microstructure, microcracks/voids, and thermal effect after irradiation was analyzed by TEM.

4 Results and Discussion

Figure 1 shows the schematic of P2 laser scribing on CdTe-based solar cells from the glass side under micro-explosion mechanism. The removal mechanism can be divided into three steps: first, the laser has been absorbed by the entire and partial layers of CdS and CdTe, respectively. The absorption depths of CdS (film thickness of 200 nm) and CdTe (film thickness of 2 μm) at the wavelength of 532 nm are ~1 μm and 167 nm, respectively. Second, as the pulse continues heating, the material in the absorption volume has been melted, vaporized, and finally formed a plasma. Due to the confinement of substrate and solid CdTe, an intensive pressure induced by the plasma expansion will pull the solid CdTe material upwards and to delaminate from CdS layer. This is because the adhesion between CdS and CdTe layers is smaller than that between SnO₂:F and CdS layers due to the differences of their thermal expansion coefficients, i.e., thermal expansion of CdTe, CdS, and SnO₂:F are 5.9 × 10⁻⁶, 4 × 10⁻⁶, and 4 × 10⁻⁶/K, respectively [28]. Third, the deformed solid CdTe layer has been removed due to brittle fracture, and the ablated material is also ejected with the pressure release to the ambient. Some resolidified molten CdS and undamaged CdS materials remain after the removal process. Due to the weak adhesion between CdS and CdTe, there is no CdTe has been melted at the boundary. In contrast, CdS removal is dominant by ablation. Therefore, thermal effect only occurs at this layer.

4.1 Film Removal by Single Pulse Irradiation

4.1.1 Scribe Geometry and Defect Characterization at a High Fluence. Figure 2(a) shows the SEM image of film removal by single pulse irradiated at a fluence of 3 J/cm². It can be seen that a near-circular area with a diameter of around 75 μm is scribed. A macrocrack occurs along the circumference of the scribed area. Magnified SEM image Fig. 2(b) shows clearly that the macrocrack occurs at the boundary is partially broken, which may be due to the nonuniform beam energy distribution of the laser spot. The material at the central area with a high-energy distribution has been removed faster than the surrounding area, and then the trapped pressure between the film and substrate is released quickly. Therefore, the significantly reduced pressure is not strong enough to fracture the rest CdTe material; instead, the pressure makes CdTe delaminate from the CdS layer and form as a macrocrack after processing. It is also observed that some material remains, which may include the undamaged CdS material and solidification of a liquid flow driven to the boundary by plasma expansion. Since the molten CdS layer is much thinner than the thickness of removal films, and the pressure distribution at the boundary is almost parallel to the film surface due to the film deformation; thus, most of the molten CdS material can be pushed to the boundary. This is why from the optical profilometry measurement along line A shown in Fig. 2(c), the circle B area shows a gradual increase to the boundary and the highest point occurs at the interface of solid/liquid CdS. Circle A shows the appearance of the macrocrack of CdTe film, and the reason why no delamination can be seen is because the detecting optical beam is perpendicular to the samples, so that the gap at the CdS/CdTe interface cannot be measured. The depth of film removal is measured to be 2 μm at the scribed center, and vertical sidewalls are formed after processing. EDX line profile scan along A is shown in Fig. 3. It can be seen that no other elements except Si and Sn in region B, which indicates that CdS and CdTe are completely removed in this region and no interdiffusion of S into the TCO layer. The co-existing of Si and Sn is due to the larger electron penetration depths of SnO₂:F compared to its thickness [13]. In region A (~10 μm)—macrocrack broken area, elements of Cd and S are

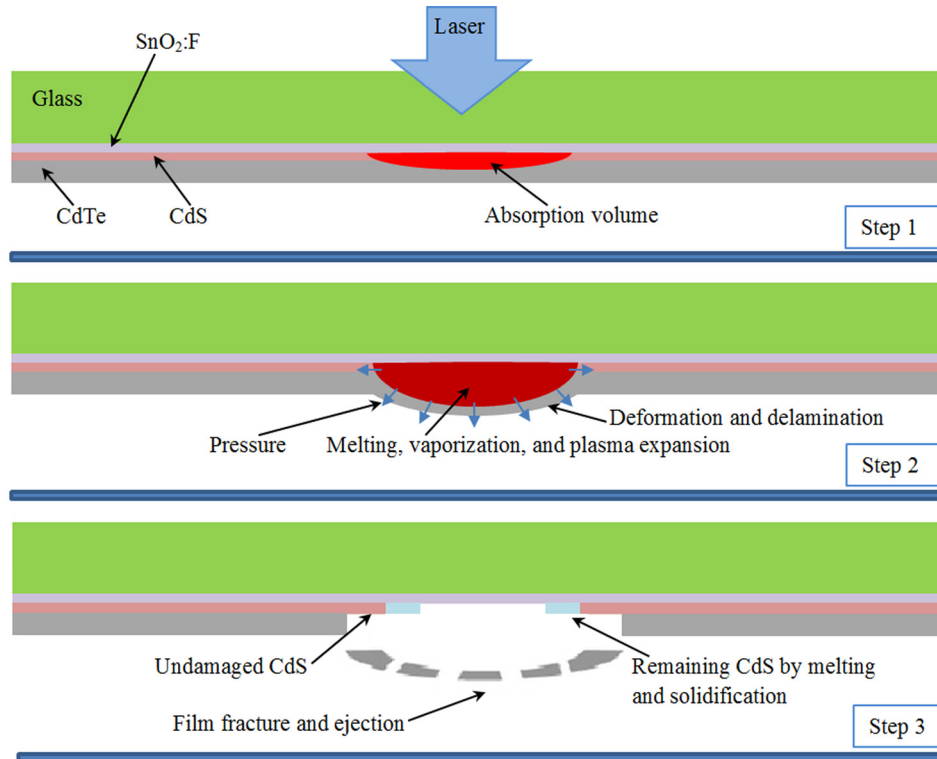


Fig. 1 Schematic of film removal of P2 laser scribing on CdTe-based solar cells under micro-explosion mechanism

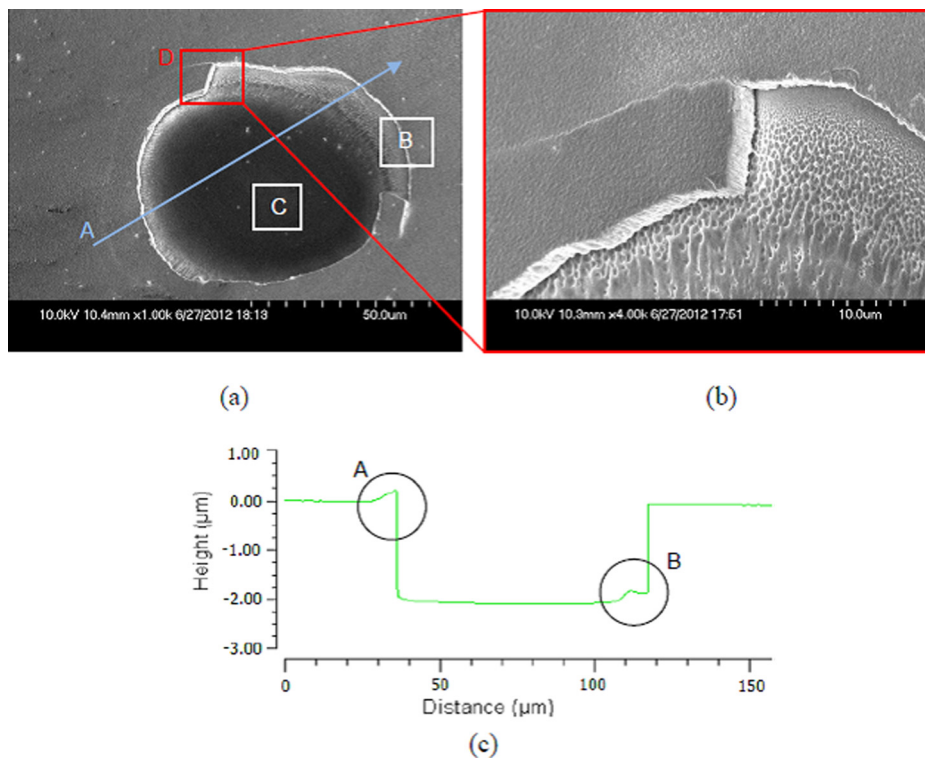


Fig. 2 (a) SEM image of film removal by a pulse irradiated at a fluence of 3 J/cm^2 ; (b) magnified SEM image at square D; and (c) optical profilometry measurement along A

detected besides Sn and Si. This demonstrates that the only CdS remains, which matches the mechanism described in Fig. 1 that higher adhesion occurs at the interface between CdS and TCO layers.

Figure 4 shows a cross-sectional TEM image of as-received samples. The thickness of CdTe, CdS, and TCO layers are measured to be $1.85 \mu\text{m}$, 230 nm , and 430 nm , respectively, which are close to the deposition estimation. CdTe grains grow epitaxially

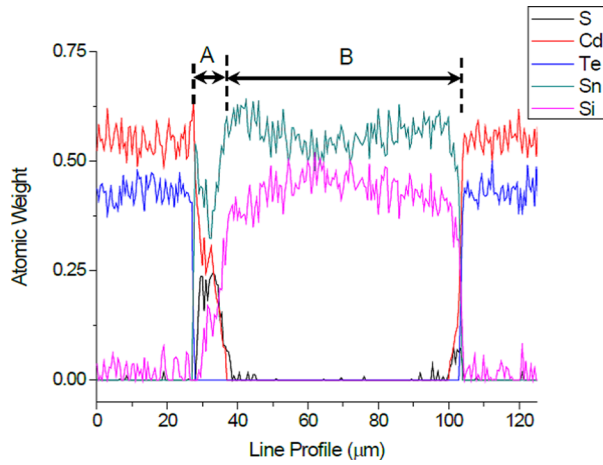


Fig. 3 EDX line profile scanning along A in Fig. 2(a), showing a clean removal at the center, and small amount of remaining material is CdS and no interdiffusion occurs at the interface of TCO/CdS

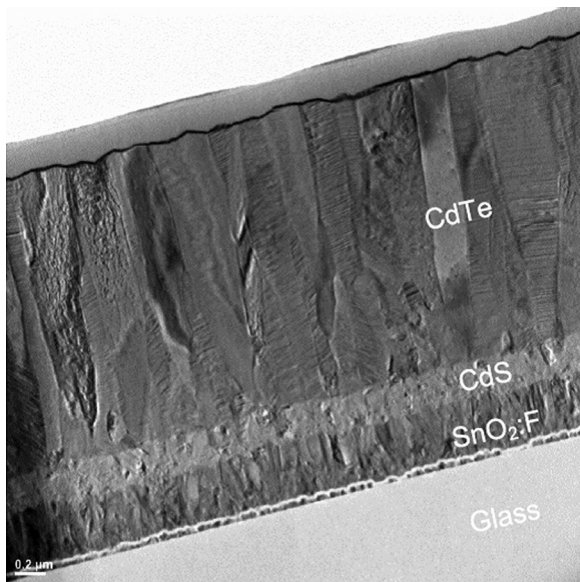


Fig. 4 Cross-sectional TEM image of as-received CdTe/CdS/TCO/glass samples

on CdS grains with a dominant orientation of (111) and the columnar CdTe grains with microtwins results in a poor photocurrent and high-series resistance [2]. Vere et al. [29] show that twinning is an intrinsic feature of the zincblende-structure materials with low-stacking fault energy, such as II-V (CdTe) and III-V semiconductors. It originates on the liquid/solid interface during growth, where group of atoms deposited at a point or points on the interface are misorientated with respect to the remainder. Figure 5 depicts the cross-sectional TEM image at the scribe boundary B shown in Fig. 2(a). It can be seen that CdTe is removed mechanically instead of thermal ablation. The pressure induced by plasma expansion causes the deformation of CdTe layer and delamination from the CdS layer. Brittle fracture sequentially occurs at high-stress concentration points at the constraint boundary. Cracks initialize at the bottom of the CdTe layer and propagate to the top surface, since the deformed geometry of boundaries causes higher material strains at the bottom compared to the top surface. The crack propagates along the grain boundary (intergranular fracture) at the bottom, because impurities usually segregate at the CdS/CdTe interface in the beginning of deposition, which weaken and

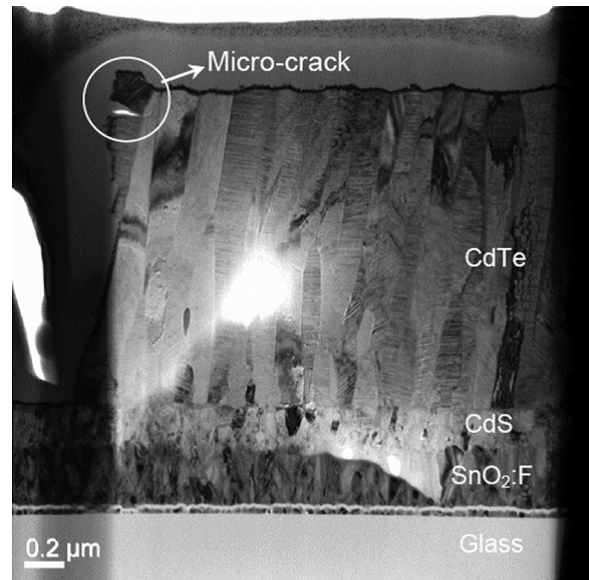


Fig. 5 Cross-sectional TEM image of scribe boundary at square B shown in Fig. 2(a), showing microcrack is formed near the top surface at the scribe sidewalls

embrittle the grain boundaries. When crack propagates to the top surface, it passes through grains (transgranular fracture) by cutting across twins. This may be caused by the direction change of the applied stress due to the film deformation and grain geometries. The stress could lead to the secondary crack along the twin boundaries and form a zig-zag scribe boundary [30]. The atomic bonding energy becomes smaller for the atoms near the top surface, and a lateral nanocrack occurs at this point simultaneously. Figure 6(a) shows that the remaining CdS layer near the sidewall has the same microstructure and thickness compared to the undamaged CdS in Fig. 4. Likewise, the TEM image of Fig. 6(b) taken at the scribe center (region C in Fig. 2(a)) exhibits that only SnO₂:F layer remains. There is no SnO₂:F has been damaged after scribing by comparing the microstructure and the material thickness. Therefore, it can be concluded that CdS material has been ablated in the laser effected area. In the meanwhile, CdTe delaminates from CdS layer and is removed due to the brittle fracture caused by the plasma-induced pressure. The thermal effect only occurs at the layer of CdS and no damage of SnO₂:F or interdiffusion of sulfur is observed after processing.

4.1.2 Scribe Geometry and Defect Characterization at a Low Fluence. Figure 7 shows the SEM image of film removal irradiated by one pulse at a fluence of 1 J/cm². It can be seen that a circular scribed area with a diameter of around 60 μm with much more remaining CdS material (determined by EDX, not shown) compared to that scribed under 3 J/cm². In addition, no macrocrack is observed in this condition. This could be caused by a longer response time of CdTe film deformation at a lower fluence, and CdTe film will delaminate more from CdS substrate and the film at the boundary and center break at the same time. In order to understand the removal mechanism, cross-sectional TEM images at the scribe boundary B' are carried out as shown in Fig. 8(a). It can be seen that a microcrack and some nanovoids appear at the CdS/CdTe interface. The CdTe layer under a lower fluence needs more time to be completely fractured. Thus, when a crack initializes at the bottom and starts propagating to the top surface, there is enough time for the pressure to causes a lateral delamination and several nanovoids along the interface of CdS and CdTe due to the weak adhesion before the entire layer has been removed. Similarly to the film removal at 3 J/cm², the remaining CdS is not thermal affected at the removal boundary and vertical sidewalls are formed. Figure 8(b) shows the magnified TEM image near

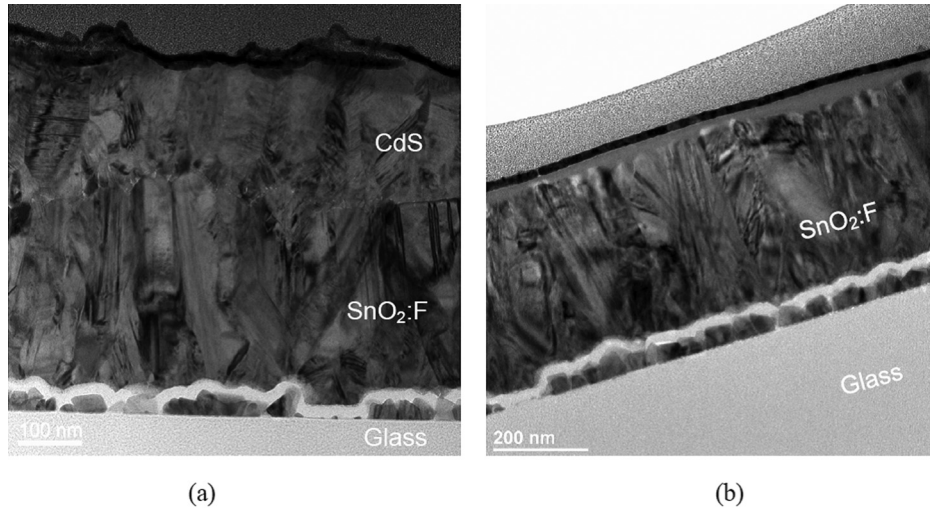


Fig. 6 Cross-sectional TEM images of (a) near scribe boundary B and (b) scribe center region C in Fig. 2(a)

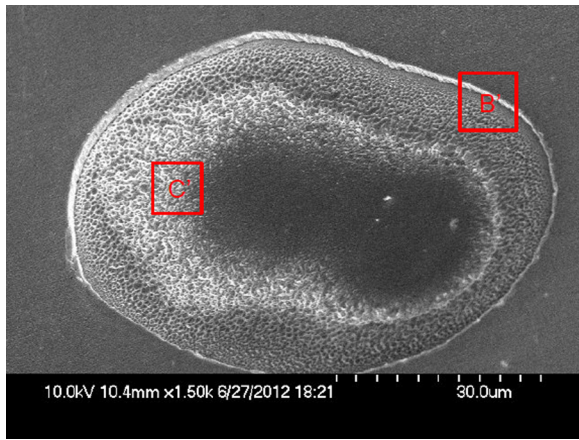


Fig. 7 SEM image of film removal by a pulse irradiated at a fluence of 1 J/cm^2 , showing much more CdS remaining after processing compared to that processed at a fluence of 3 J/cm^2

delamination tip. It can be observed that the high-stress concentration at the tip causes change of atomic structures at both CdS and CdTe grain boundaries and interface. Moreover, nanocracks are founded around the nanovoids (not shown). These phenomena suggest that those dislocation slips, caused by the atomic structure rearrangements, may play an important role on the further crack initiation and propagation [31] and then reduce the power output resulting in a long-term instability. Cross-sectional TEM image taken at region C' in Fig. 7 is shown in Fig. 9(a). It can be seen that both microstructures and thickness of CdS layer have been changed due to the thermal effect. The arrow shows the direction to the removal boundary. The molten CdS material solidifies and the grain grows vertically from SnO₂:F layers near the boundary; however, the grains close to the center shown in Fig. 9(b) exhibit different microstructures and nanobubbles near the interface. The grain size in this region is much smaller (a few nanometers) based on high-resolution TEM investigation (not shown). The thermal gradient in the molten pool drives the motion of liquid CdS provoking the deformation of the surface, and the pressure differences created at a curved interface support the evolution of the deformation on the liquid surface known as capillary waves [17]. However, due to the plasma expansion and micro-explosion process, the pressure propagated along horizontal direction pushes

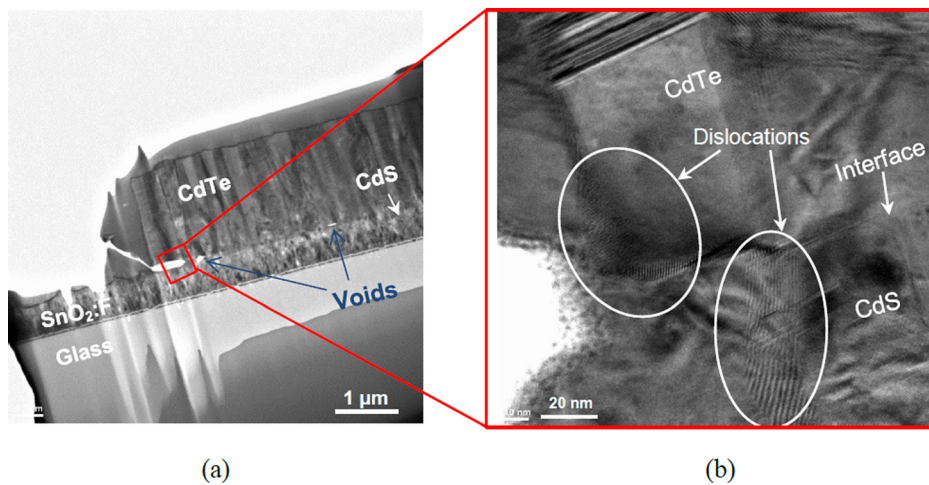


Fig. 8 Cross-sectional TEM images of (a) scribe boundary at square B' shown in Fig. 7 and (b) magnified image at the delamination tip, showing dislocations formed at both between the two layers and grains which may introduce further crack initiation

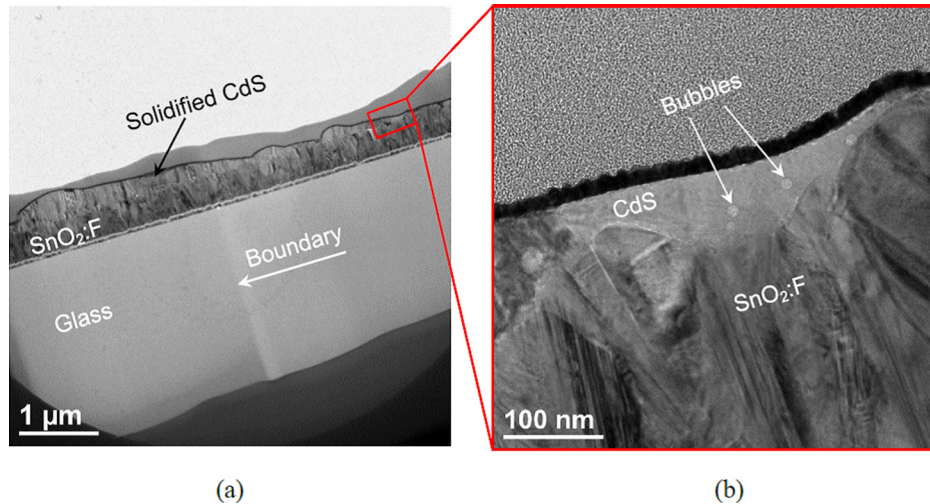


Fig. 9 (a) TEM images taken at region C' in Fig. 7 and (b) magnified TEM image at the interface between CdS and SnO₂:F layers, showing nanobubbles formed due to the oxidation of sulfur during the laser processing

more liquid CdS to the boundary and forms the different amplitudes along the capillary wave. The liquid CdS close to the center under stronger pressure travels a longer distance; thus, there is not enough time for a similar recrystallization process to that happened near the boundary. Moreover, decomposition of CdS occurs due to the high temperature, and sulfur can be quickly oxidized and formed as gaseous phase. Sulfur oxide either evaporates to the environment or stay inside the CdS matrix to form as bubbles after solidification.

Overall, scribing under both two fluences can achieve a complete film removal, and no damage of SnO₂:F or interdiffusion of sulfur occurs after processing. However, some CdS remains and partial of the material has been melted and recrystallized. This will affect the next-step contact layer deposition in the solar cell fabrication process. In addition, the ultrafast heating process could introduce supercooling during recrystallization, which causes defects as recombination centers and reduces the photocurrent density. Moreover, the bubbles formed by sulfur oxide will also introduce abnormal heating and eventually damage the cells [22]. Scribing under a high fluence can cause macrocracks due to the pulse imperfection and microcracks near the top surface which may decrease the active area of absorber layers. However, scribing under a low fluence can lead to more remaining CdS material, which can cause a higher increase of contact resistances between TCO and metal layers. The film delamination will lead to an increase of inactive cells.

In order to understand the relationship between the induced defects and scribing conditions, a parametric study is carried out on the irradiation fluences (0.8 J/cm² to 6 J/cm²) as shown in Fig. 10. Since the pulse shape is irregular, normalized diameters are calculated through the measurement of scribe areas. From the observation under SEM and optical profilometry, the threshold for complete removal is 0.8 J/cm². The scribe diameter increases with the increasing fluence at range A (0.8 to 2.2 J/cm²) and keeps a constant around 75 μm at range B (2.2 to 4 J/cm²) and then increase at fluence range C (4 to 6 J/cm²). This difference is because in the low-fluence range, the film breaks at both boundary and center at a close time interval due to the longer removal time. In contrast, the center is removed much faster than the boundary when the fluence reaches a center threshold, and the reduced pressure cannot delaminate more CdTe material from CdS layer. The trend of scribe diameter increases again at fluence range C. This is due to absorption volumes become larger under higher fluences; therefore, the sequential plasma volume increases and more material will be removed. In addition, the increased pressure in lateral

direction could cause solid CdS and CdTe material to fracture, which leads to an increase of scribe areas. The percentage of residual CdS area linearly decreases with increasing of fluences at the low-fluence range A, and keeps a constant at fluence range B, and finally slightly decreases at the fluence range C. The laser-induced pressure becomes larger and larger with increasing fluences during micro-explosion processes; thus, more liquid CdS is driven to the boundary and less CdTe delaminates from the CdS layer due to faster brittle-fracture responses. Until the pressure reaches a threshold, all liquid CdS moves to the boundary and cannot flow out of the removal cavity by the prevention of CdTe layer.

4.2 Numerical Investigation on Film Removal and Defect Formation.

Two-dimensional thermal and mechanical models are setup based on the previous study [13], except adding a CdS layer in the thermal model to determine the plasma volume and considering dynamic response in CdTe fracture criteria. Figure 11 shows the temperature distribution of CdTe/CdS/SnO₂:F stack layers on glass substrate as a result of the glass-side laser irradiation at a fluence of 1 J/cm². The thicknesses of different layers are 2 μm, 200 nm, 400 nm, and 50 μm, respectively. The laser pulse is 9 ns in duration, Gaussian-distributed, 50 μm in spot size, and

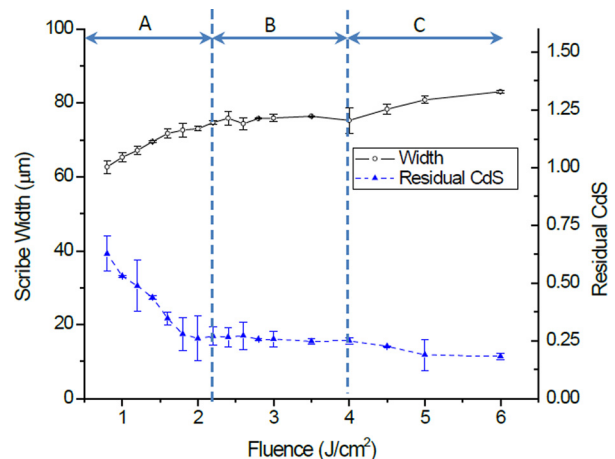


Fig. 10 Dependence of scribe area and remaining CdS on laser irradiation conditions, error bars represent standard deviation

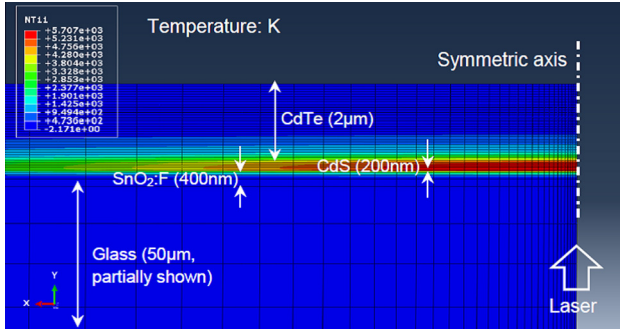


Fig. 11 Simulation result of temperature distribution of CdTe/CdS/SnO₂:F/glass multilayer thermal model at a fluence of 1 J/cm²

532 nm in wavelength. The thermal analysis is carried out with the consideration of energy loss due to the reflection at the interfaces of glass/air, glass/SnO₂:F, and SnO₂:F/CdS, heat convection at the boundary, as well as the absorption by the glass substrate and SnO₂:F layer. Material properties can be found in Ref. [13]. It can be observed that the absorbing volume is confined between the CdTe and SnO₂:F layers, and the temperature is almost uniformly distributed in CdS layer due to its absorption depth and thickness as discussed before. This highly confined energy increases temperature up to 8000 K at this condition, which is higher than the vaporization temperatures of both CdTe and CdS, therefore, plasma has been generated. The temporal and spatial distributions of plasma-expansion-induced pressure are then calculated based on Ref. [13], and the constant fraction α is kept 0.04 to match the removal threshold compared to experimental results. Figure 12 shows the highest temperature of TCO layer at different conditions for estimating its thermal damage. The temperature is recorded when the film starts detaching from the TCO layer which is determined through the mechanical model, since there is no film deformation considered in the thermal model. It can be seen that the TCO temperature increases with the increasing of fluences and reaches the melting temperature at a fluence of 5.5 J/cm².

Film removal is presented in a mechanical model with the pressure incorporated on CdTe layer at the interface. A 10 nm-thick layer of cohesive elements is implemented to consider the traction stresses at the interface. The cohesive layer is governed by the traction separation law described in Ref. [13] and serves the purpose of simulating the process in which the CdTe film lifts up and delaminates from the CdS layer caused by the plasma expansion.

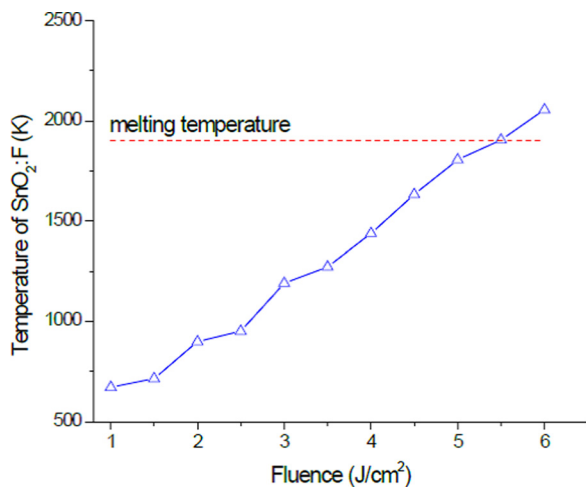


Fig. 12 Simulation results of dependence of SnO₂:F (TCO) temperature on fluence, showing the TCO layer will be damaged when the fluence reaches 5.5 J/cm²

In order to simplify the problem, CdS is neglected from the mechanical model. Because CdS layer is dominantly removed by ablation based on experimental results, there is no effect of mechanical fracture on this layer during micro-explosion process. Since adhesion becomes zero at the plasma area, an open cavity at the center of the cohesive layer, representing plasma width, is implemented. The values of plasma width are extracted from the thermal model. The pressure is applied at the interface of CdTe and cohesive layer, and the pressure is set to be zero when the film is broken during the calculation and the boundaries are fixed.

Figure 13 shows the complete film removal with a fluence of 1 J/cm² at 97.9 ns. It can be seen that a scribe area with a radius of 28.7 μ m and a delamination of 2.8 μ m at the interface. Therefore, film delamination occurs compared to the initial plasma width of 41.6 μ m. This matches the experimental result as shown in Fig. 8(a). The simulation result shows that the strain rate of failed elements is up to 10⁵ s⁻¹. Therefore, the material dynamic response is necessary to be implemented. The film is removed mainly due to the tensile stress, and the strain-rate-dependent response has much less influence on the tensile yield stress than the compressive yield stress for brittle materials. However, the implemented criteria can still affect the compressive failure and lead to more accurate element deformations compared the static fracture laws. The film deformation causes tensile stress to the elements at the top center and bottom boundary. Therefore, the fracture occurs preferentially at these points. Since the pressure is not strong enough to break the entire layer immediately, a further delamination along the interface occurs due to its weak adhesion. The film still remains large pieces when the removal is completed and the breaks occur at both center and boundary. Figure 14

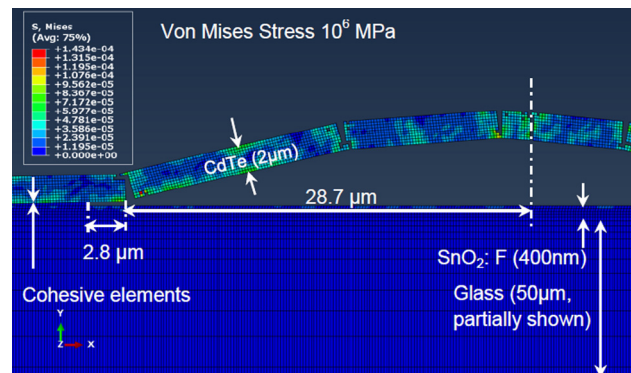


Fig. 13 Complete film removal with a fluence of 1 J/cm² at 97.9 ns, the scribe radius is 28.7 μ m, and delamination is 2.8 μ m through the interface

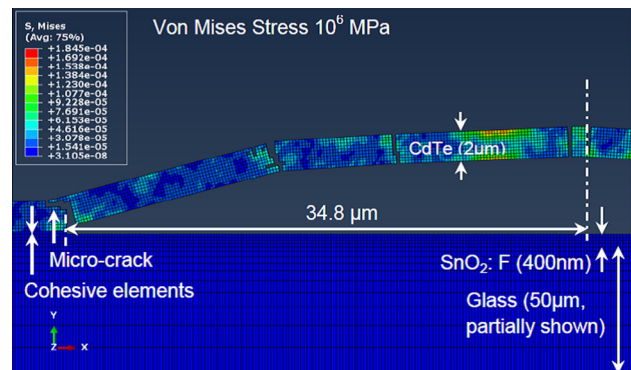


Fig. 14 Complete film removal with a fluence of 3 J/cm² at 76.8 ns, the scribe radius is 34.8 μ m, and microcrack with a length of 1.4 μ m occurs near the top surface

shows the complete film removal at a fluence of 3 J/cm^2 . It can be seen that a scribe area with a radius of $34.8 \mu\text{m}$ (plasma width is $58.8 \mu\text{m}$) and this removal takes 76.8 ns , which occurs faster than that happened at 1 J/cm^2 . Similarly, initial fractures occur at the bottom boundary and top center. However, since the pressure is strong enough to cause further deformation, some elements between the boundary and center also achieve their fracture limit. Likewise, more and more elements between those “prefracture” points fail and finally, the film becomes many small pieces after removal. At the boundary, microcracks with a length of $1.4 \mu\text{m}$ occur near the top surface rather than at the interface. During the crack propagates through the boundary from bottom to the top, the stress induced by the pressure and film deformation is strong enough to fracture their neighboring elements so that the microcrack preferentially occurs at a relatively weak bonding area near the top surface, which has been presented in Fig. 5.

Figures 15 and 16 show the simulation results of dependence of plasma width, scribe diameter, and remaining CdS on laser irradiation fluences. Residual CdS is defined as the ratio between area of residual CdS and area of laser scribe. Since the pressure is only applied vertically in the mechanical model, much less pressure in lateral direction in the simulation, thus, the model cannot well-predict the lateral material fracture when the fluence is larger than

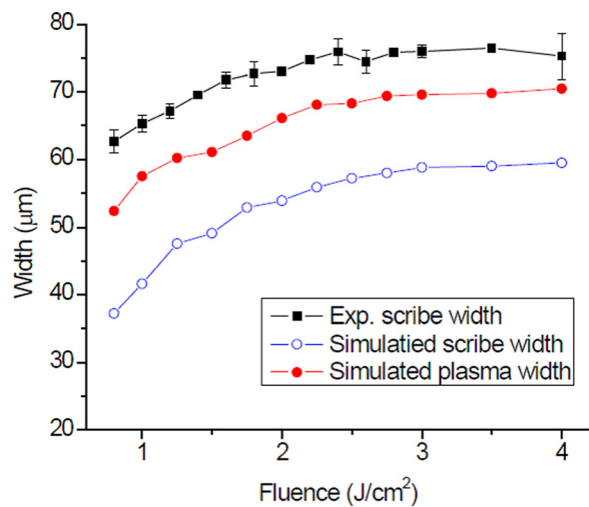


Fig. 15 Comparison of experimental and simulation results on scribe width, error bars represent standard deviation

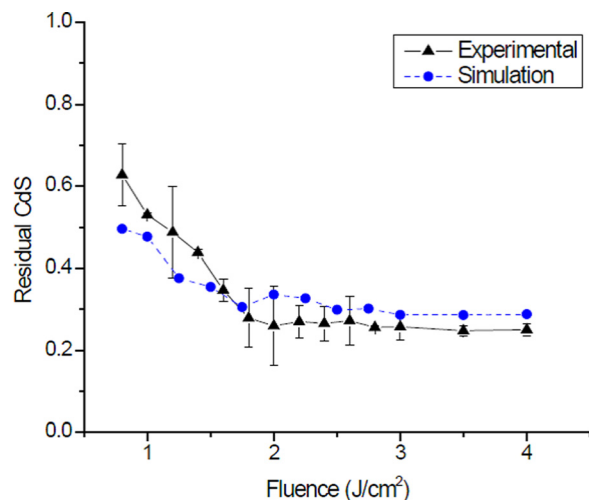


Fig. 16 Comparison of experimental and simulation results on residual CdS, error bars represent standard deviation

4 J/cm^2 as shown in Fig. 10. In addition, these increased scribe widths at higher fluences enlarge the dead zone. Therefore, a narrower fluence range (0.8 J/cm^2 to 4 J/cm^2) is taken in the simulation. It can be seen that the plasma width increases to around $55 \mu\text{m}$ at 2.5 J/cm^2 and maintains almost a constant afterwards. Compared to the spot size ($50 \mu\text{m}$), only $2.5 \mu\text{m}$ -wide CdS material in lateral direction has reached the vaporization temperature beyond the laser irradiation area. This presents the laser-induced heat can only be transferred laterally close to CdTe film thickness ($2 \mu\text{m}$), because it is dissipated quickly to the ambient at the top of CdTe layer. Therefore, the plasma width increases much slowly when it reaches the spot size. The simulation result shows the scribe diameter has a similar trend to that of plasma widths. At the low-fluence range, more CdTe material delaminates from the layer underneath, since it takes more time for the film to deform before entire layer is fractured. In contrast, at the high-fluence range, the scribe width keeps a constant, because the pressure is strong enough to fracture the entire film immediately and there is no time to lead to further film deformation and delamination. The percentage of residual CdS material shows a similar trend to the experimental result, more CdS remains in the low-fluence range and finally it keeps a constant in the high-fluence range. The discrepancy of an underestimation at the low-fluence range in the simulation could be caused by ignoring the thermal effect on the cohesive elements, since the adhesion decreases with the increasing of the temperature. The overestimation at the high-fluence range could be due to the ignoring of the molten CdS movement by the lateral pressure. However, the overall fluence dependence on film removal by micro-explosion is accurately captured by the simulation. Figure 17 shows the simulation results of crack and delamination lengths after laser scribing. It can be seen that the delamination exists when the fluence is lower than 2.5 J/cm^2 and microcracks are remained at higher conditions. The delamination lengths are higher than that of the microcracks which shows the similar results of the cross-sectional TEM images. Those cracks and delamination will cause inactive cells and increase the dead zones. Therefore, a minimum crack length at a fluence of 3 J/cm^2 is more desirable for the scribing conditions.

4.3 Line Scribing and Sheet Resistance Measurement. In order to optimize the line scribing condition, samples are processed at the fluence values from 1 to 4 J/cm^2 with different speeds from 1 to 4 mm/s , which equivalent to the pulse overlapping from 80% to 20%. Among the complete removal conditions, the highest speed occurs at 2 mm/s under a fluence of 3 J/cm^2 as shown in Fig. 18(a). It can be seen a clean line is formed in a width of

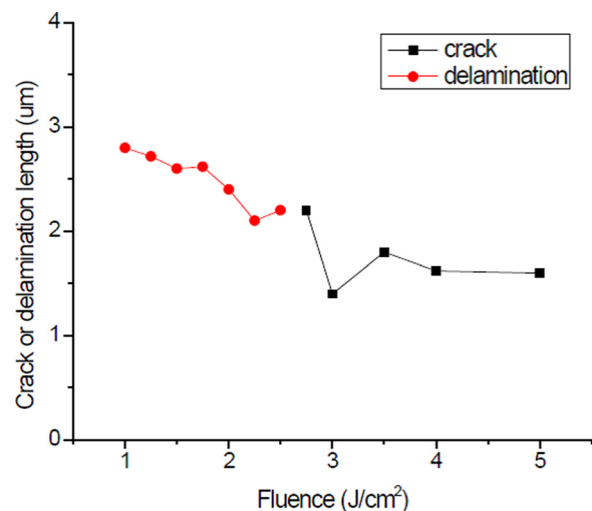


Fig. 17 Simulation results of microcrack and delamination lengths after laser scribing

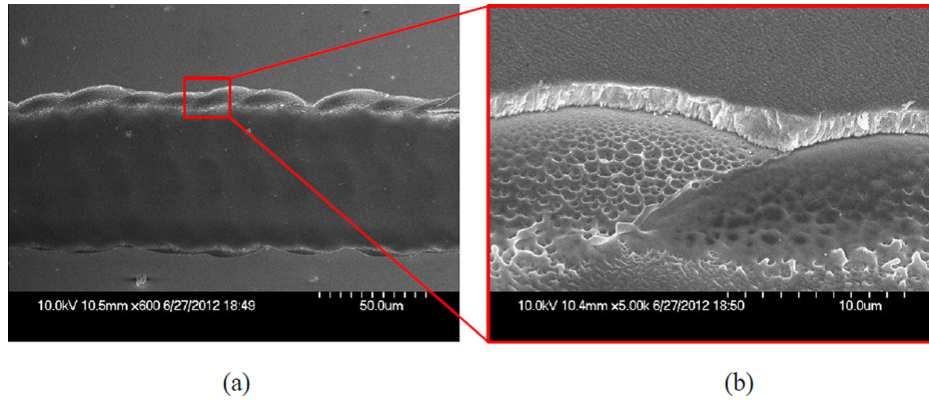


Fig. 18 SEM images of (a) line scribing at a fluence of 3 J/cm^2 and a speed of 2 mm/s and (b) magnified image at scribe boundary, showing macrocracks are removed due to the pulse overlapping

$\sim 75 \mu\text{m}$. Figure 18(b) shows that macrocracks are removed by the next overlapped pulse at the removal boundary. Although the scribing speed is not in the desirable range (m/s) due to the limitation of pulse repetition rate, the experimental results can still be referenced with different laser facilities based on the fluence and pulse overlapping.

Based on the line scribing results, an area of $5 \text{ mm} \times 20 \text{ mm}$ is scribed with different fluences at a speed of 2 mm/s and 50% line overlap. The sheet resistance measurement results are shown in Fig. 19. The sheet resistance measurement reflects the cleanliness of the laser scribing, which will significantly affect the contact resistance between the further deposited metal layer and the TCO layer. Since contact resistance is partial of series resistance of a solar panel, the increased contact resistances in a large number of scribing lines will severely reduce the panel efficiency. Higher resistances can be caused by the residual material at lower fluences (1 J/cm^2 to 4 J/cm^2) or the damage of TCO materials at higher fluences (5 J/cm^2 to 6 J/cm^2). This TCO damage threshold is close to that of 5.5 J/cm^2 predicted in the simulation shown in Fig. 12. The discrepancy could be caused by neglecting the heat conduction between the plasma and TCO layer after the film detaching. It can be seen that the contact resistance achieves 4 orders of magnitude due to the damage of TCO materials compared to that at the lower fluence range. The contact resistance reaches the minimum value at 3 J/cm^2 , which is even a bit lower than that measured

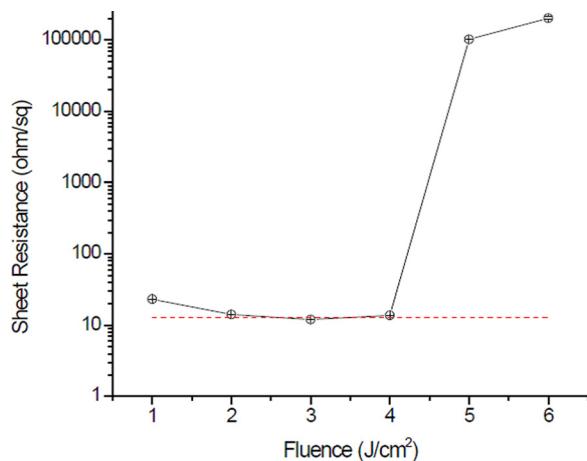


Fig. 19 Dependence of sheet resistances on fluence. The high resistance at low-energy range is due to the residual CdS, and high resistance at high-energy range is caused by the TCO damage. Dashed line represents the sheet resistance of TCO material only and error bars represent standard deviations.

from TCO material only (samples of TCO deposited on glass substrate). Therefore, it can be concluded that the condition of 3 J/cm^2 with a scribing speed of 2 mm/s is the optimal processing condition for P2 laser scribing of CdTe-based solar cells.

5 Conclusion

In conclusion, it has been demonstrated that successfully selective film removal with well-defined sidewalls and little thermal effect is achieved by glass-side laser scribing of CdTe-based multilayer solar cells. The micro-explosion mechanism only leads melting and recrystallization on CdS layer, which could cause defect generation under the supercooling process. CdS material is removed dominantly through ablation because its absorption depth is much larger than the thickness. In contrast, the rest of laser energy is fully absorbed by a shallow layer in the CdTe film. Due to the confinement of solid CdTe and the substrate, a shock wave is generated caused by the plasma expansion and CdTe material is removed through brittle fracture by the induced pressure. CdTe film delimitation from the CdS layer is also observed due to the weaker adhesion between these two layers compared to other interfaces, which will affect the next-step contact layer deposition in the solar cell fabrication process. Furthermore, other defects are characterized under both low and high-fluence ranges. These defects, including nanobubbles caused by sulfur oxidation, microcracks, dislocation formed at delamination tips due to the atomic structure rearrangement, could further induce abnormal heating and poor photocurrent. The optimal condition (with minimum defects at the scribe boundary and minimum sheet resistance in the scribe area) of glass-side laser scribing is determined to be at a fluence of 3 J/cm^2 with a speed of 2 mm/s . The low-scribing speed is limited by the pulse repetition rate; however, the experimental results are still valuable for the investigation on different required laser facilities. Finally, numerical finite-element models are developed for P2 scribing based on micro-explosion mechanism. Good agreements with experimental results show that the simulation is capable of predicting the material removal dynamics and fracture behavior of CdTe.

Acknowledgment

Research carried out in part at the Center for Functional Nanomaterials, Brookhaven National Laboratory, which was supported by the U.S. Department of Energy, Office of Basic Energy Sciences, under Contract No. DE-AC02-98CH10886. We must appreciate Technical Associate, Kim Kisslinger, Center for Functional Nanomaterials, Brookhaven National Laboratory, for his guidance and help with TEM sample preparation and imaging. The use of material characterization equipment at Materials Research Science and Engineering Center, Columbia University is also

gratefully acknowledged. Thanks are due to Dr. Marco Leona and Dr. Pablo Londero, Department of Scientific Research, the Metropolitan Museum of Art, for processing equipment use.

References

- [1] Dhere, R. G., Bonnet-Eymard, M., Charlet, E., Peter, E., Duenow, J. N., Li, J. V., Kuciauskas, D., and Gessert, T. A., 2011, "CdTe Solar Cell With Industrial Al:ZnO on Soda-Lime Glass," *Thin Solid Films*, **519**(21), pp. 7142–7145.
- [2] Luque, A., and Hegedus, S., 2003, *Handbook of Photovoltaic Science and Engineering*, Wiley, Chichester, UK.
- [3] Booth, H., 2010, "Laser Processing in Industrial Solar Module Manufacturing," *J. Laser Micro/Nanoeng.*, **5**(3), pp. 183–191.
- [4] Compaan, A. D., and Matulionis, S. N., 2000, "Laser Scribing of Polycrystalline Thin Films," *Opt. Lasers Eng.*, **34**(1), pp. 15–45.
- [5] Murison, R., Dunsky, C., Rekow, M., Dinkel, C., Pern, J., Mansfield, L., Panarello, T., and Nikumb, S., 2010, "CIGS P1, P2 and P3 Laser Scribing With an Innovative Fiber Laser," 35th IEEE Photovoltaic Specialists Conference, Honolulu, HI, June 20–25, pp. 179–184.
- [6] Bovatsek, J., Tamhankar, A., Patel, R. S., Bulgakova, N. M., and Bonse, J., 2010, "Thin Film Removal Mechanisms in ns-Laser Processing of Photovoltaic Materials," *Thin Solid Films*, **518**(10), pp. 2897–2904.
- [7] Dunsky, C. M., and Colville, F., 2008, "Scribing Thin-Film Solar Panels," Industrial Laser Solutions for Manufacturing.
- [8] Gecys, P., and Raciukaitis, G., 2010, "Scribing of a-Si Thin Film Solar Cells With Picoseconds Laser," *Eur. Phys. J. Appl. Phys.*, **51**(3), p. 33209.
- [9] Wang, W., Wang, K. D., Jiang, G. D., Mei, X. S., and Yang, C. J., 2010, "Comparison of Femtosecond Laser-Induced Front- and Rear-Side Ablation of Films," *Proc. Inst. Mech. Eng., Part B*, **225**(4), pp. 520–527.
- [10] Beyer, S., Tonrnari, V., and Gornicki, D., 2003, "Comparison of Laser Induced Front- and Rear Side Ablation," *Proc. SPIE*, **5063**, pp. 202–207.
- [11] Sano, T., Yamada, H., Nakayama, T., and Miyamoto, I., 2002, "Laser Induced Rear Ablation of Metal Thin Films," *Proc. SPIE*, **4426**, pp. 70–73.
- [12] Matylitsky, V. V., Huber, H., and Kopf, D., 2011, "Selective Removal of Transparent Conductive Oxide Layers With Ultrashort Laser Pulses: Front- vs. Back-Side Ablation," International Congress on Applications of Lasers and Electro-Optics, pp. 1022–1027.
- [13] Wang, H., Hsu, S., Tan, H., Yao, Y. L., Chen, H., and Azer, M., 2013, "Predictive Modeling for Glass-Side Laser Scribing of Thin Film Photovoltaic Cells," *ASME J. Manuf. Sci. Eng.*, **135**(5), p. 051004.
- [14] Shinohara, W., Shima, M., Taira, S., Uchihashi, K., and Terakawa, A., 2006, "Applications of Laser Patterning to Fabricate Innovative Thin-Film Silicon Solar Cells," *Proc. SPIE*, **6107**, p. 61070J.
- [15] Kontgers, M., Kunze, I., Kajari-Schroder, S., Breitenmoser, X., and Bjorneklett, B., 2010, "Quantifying the Risk of Power Loss in PV Modules Due to Micro Cracks," 25th European Photovoltaic Solar Energy Conference, Valencia, Spain, pp. 3745–3752.
- [16] Tull, B. R., Carey, J. E., Mazur, E., McDonald, J. P., and Yalisove, S. M., 2006, "Silicon Surface Morphologies After Femtosecond Laser Irradiation," *MRS Bull.*, **31**(8), pp. 626–633.
- [17] Wang, H., Lusquiños, F., and Yao, Y. L., 2012, "Effect of Hydrogen on Surface Texturing and Crystallization of a-Si:H Thin Film Irradiated by Excimer Laser," *Appl. Phys. A*, **107**(2), pp. 307–320.
- [18] Wang, H., Kongsuwan, P., Satoh, G., and Yao, Y. L., 2012, "Femtosecond Laser-Induced Simultaneous Surface Texturing and Crystallization of a-Si:H Thin Film: Absorption and Crystallinity," *ASME J. Manuf. Sci. Eng.*, **134**(3), p. 031006.
- [19] Borrajo, J., Vetter, M., and Andreu, J., 2009, "Laser Scribing of Very Large 2.6 m × 2.2 m a-Si:H Thin Film Photovoltaic Modules," 2009 Spanish Conference on Electron Devices, Santiago de Compostela, Spain, pp. 402–405.
- [20] Lauzurica, S., Garcia-Ballesteros, J. J., Colina, M., Sanchez-Aniorte, I., and Molpeceres, C., 2011, "Selective Ablation With UV Lasers of a-Si:H Thin Film Solar Cells in Direct Scribing Configuration," *Appl. Surf. Sci.*, **257**(12), pp. 5230–5236.
- [21] Tomaoki, S., Kaneuchi, Y., Kakui, M., Baird, B., Paudel, N., and Wieland, K., 2010, "Development of Wide Operational Range Fiber Laser for Processing Thin Film Photovoltaic Panels," 29th International Congress on Applications of Laser & Electro-Optics, Anaheim, CA, p. M1306.
- [22] Acciani, G., Falcone, O., and Vergura, S., 2010, "Defects in Poly-Silicon and Amorphous Silicon Solar Cells," International Conference on Renewable Energy and Power Quality, Spain.
- [23] Golovan, L., Kashkarov, P., and Timoshenko, V., 1996, "Laser-Induced Melting and Defect Formation in Cadmium Telluride," *Laser Phys.*, **6**(5), pp. 925–927.
- [24] Emel'yanov, V. I., and Kashkarov, P. K., 1992, "Laser-Induced Defect Formation in Semiconductors," *Appl. Phys. A*, **55**(2), pp. 161–166.
- [25] Addeision, F. L., and Johnson, J. N., 1990, "A Constitutive Model for the Dynamic Response of Brittle Materials," *J. Appl. Phys.*, **67**(7), pp. 3275–3286.
- [26] Holmquist, T. J., and Johnson, G. R., 1994, "An Improved Computational Constitutive Model for Brittle Materials," AIP Conf. Proc. **309**(1), pp. 981–984.
- [27] Holmquist, T. J., and Johnson, G. R., 2005, "Characterization and Evaluation of Silicon Carbide for High-Velocity Impact," *J. Appl. Phys.*, **97**(9), p. 093502.
- [28] Hodges, D. R., Palekis, V., Bhandaru, S., Singh, K., Morel, D., Stefanakos, E. K., and Ferekides, C. S., 2009, "Mechanical Properties and Adhesion of CdTe/CdS Thin Film Solar Cells Deposited on Flexible Foil Substrates," Material Research Society Symposium Proceedings, Vol. 1165, Paper No. 1165-M02-09.
- [29] Vere, A. W., Cole, S., and Williams, D. J., 1983, "The Origins of Twinning in CdTe," *J. Electron. Mater.*, **12**(3), pp. 551–561.
- [30] Hughes, G. M., Smith, G. E., Flewitt, P. E. J., and Crocker, A. G., 2007, "The Brittle Fracture of Polycrystalline Zinc," *Proc. R. Soc. A*, **463**, pp. 2129–2151.
- [31] Hai, S., and Tadmor, E. B., 2003, "Deformation Twinning at Aluminum Crack Tips," *Acta Mater.*, **51**(1), pp. 117–131.